CrystEngComm

Cite this: *CrystEngComm*, 2011, **13**, 5956

www.rsc.org/crystengcomm

PAPER

Self-assembled bismuth telluride films with well-aligned zero- to three-dimensional nanoblocks for thermoelectric applications†

Hsiu-Cheng Chang and Chun-Hua Chen*

Received 23rd March 2011, Accepted 10th June 2011
DOI: 10.1039/c1ce05350g

The dimension and size of the building blocks as well as the preferential orientation, geometry and regularity of their assemblies are the most important key factors for fabricating thermoelectric materials with a high figure-of-merit (ZT) which is governed by the efficiencies in transporting electrical and thermal energies along the measurement direction. A one-step and large-area growth approach has been successfully developed employing pulsed laser deposition (PLD) for producing physically self-assembled and well-aligned Bi_2Te_3 nanostructures on SiO_2/Si substrates without pre-built templates or catalysts. The precisely parameter-controlled growth provides four highly reproducible and significant Bi_2Te_3 assemblies, comprising 0-dimensional (0-D) nanoparticles, 1-D nanorods, 2-D nanoflakes, and 3-D nanocanyons, respectively exhibiting an overall (006), (015), (110), and (006) preferential orientation normal to the substrate surface. The nanoparticle assisted crystal growth is proposed, mainly involving the condensation of the plasma species in the gas phase at higher ambient pressures and the following diffusion and reorganization of the deposited nanoparticle atoms on the substrates. The well-aligned 0-D to 3-D Bi_2Te_3 nanostructures show more excellent in-plane power factors than most of the randomly aligned Bi_2Te_3 nanostructures at room temperature mainly due to significantly reducing inter resistance. The thermoelectric properties of these well-aligned Bi_2Te_3 nanostructures are comparable to any other intrinsic Bi_2Te_3 nanostructures that have ever been reported. The present data are valuable for further improving and designing advanced thermoelectric materials and confirm that precise control of nanostructural aggregation is an effective strategy for enhancing the thermoelectric performance.

Introduction

Nanostructuring has been widely accepted as one of the most effective strategies for significantly increasing the thermoelectric figure of merit $ZT = \sigma S^2 T \kappa^{-1}$ where σ is the electrical conductivity, S is the Seebeck coefficient, T is the absolute temperature, and κ is the thermal conductivity.[1–3] The product σS^2 is defined as the thermoelectric power factor. The theoretical studies of bismuth telluride (Bi_2Te_3) have obviously predicted the importance of controlling size and dimension.[4,5] For instance, the ZT for a 2-D quantum well (3.8 Å thickness) and a 1-D quantum wire (squared cross-section of 5 Å width) is about 16 and 27 times higher, respectively, comparing with that for bulk ($ZT \approx 0.52$). Experimental data for single quantum crystals are extremely lacking due to the technological difficulties of the thermoelectric measurements of such small crystals. Balandin *et al.* experimentally proved that an about 30–40% enhancement in ZT for an ultra-thin quasi-2D Bi_2Te_3 crystal was mainly contributed from the great drop of the thermal conductivity from 0.5–0.6 W m^{-1} K^{-1} (bulk) to 0.1–0.3 W m^{-1} K^{-1} in the cross-plane direction at room temperature.[6] The presence of boundaries or interfaces accompanying the decreased size or dimension is considered to be the key to effectively inhibit not only the thermal conductivity but usually also the electrical conductivity. A remarkable electrical conductivity thus is helpful to approach a high ZT for quantum crystals because of the competition relation between these two parameters as described above. It has been reported that a single Bi_2Te_3 nanowire (77 nm diameter) can present a high electrical conductivity (860 S cm^{-1})[7] which is at the same order of magnitude compared to that obtained from the bulk (900 S cm^{-1}).[8] In this case, in comparison with Bi_2Te_3 bulk, a higher ZT may be found owing to an expected lower thermal conductivity.

Even though individual Bi_2Te_3 quantum crystals have experimentally and theoretically demonstrated excellent thermoelectric performance, there still exist many technological problems in fabrication as well as characterization for further applications. Assembling the quantum crystals, *i.e.* a film or bulk with nanostructures, thus becomes a much more feasible way for

Department of Materials Science and Engineering, National Chiao Tung University, 1001 Ta-Hsueh Road, Hsin-Chu, Taiwan, 30010, R.O.C. E-mail: ChunHuaChen@mail.nctu.edu.tw; Fax: +886-3-5724727; Tel: +886-3-5131287

† Electronic supplementary information (ESI) available. See DOI: 10.1039/c1ce05350g

fundamental studies and practical applications. It is believed that orderly assembling of the nanostructures may be an advanced strategy for novel thermoelectric materials and devices since the electrical and thermal energy can be effectively transported in the orderly structures.[9,10] For a practical example, the breakthrough of the Bi_2Te_3/Sb_2Te_3 superlattices ($ZT \approx 2.4$) was considered as the result of an effective increase of the state density near the Fermi level and the phonon transport resistance contributed by the quantum confinement effect.[11] Due to these exhilarating investigations, many efforts have focused on the preparation of assemblies of Bi_2Te_3 nanocrystals with various morphologies, *e.g.* nanoparticles,[12–14] nanowires,[9,15] nanorods,[10,16] and nanoplates,[17,18] to introduce the spatial confinement. However, till now, most cases of the nanocrystal assemblies are randomly aligned to the substrates. It is hence not easy to obtain predicted significant thermoelectric properties. Well-aligned Bi_2Te_3 nanostructures prepared by template- or catalyst-free approaches were less reported. Additionally, Bi_2Te_3 nanostructures with spatial confinements from 1-D to 3-D nanocrystals also have not been systematically fabricated and studied yet. These technological issues indeed need to be clarified for the further enhancement of thermoelectric materials.

In this work, we present an optimized one-step, large-area, noncatalytic and template-free growth approach to distinct Bi_2Te_3 nanostructures by pulsed laser deposition (PLD). By optimizing the substrate temperature and background atmosphere, four physically self-assembled and well-aligned Bi_2Te_3 nanostructured films respectively consisting of 0-D nanoparticles, 1-D nanorods, 2-D nanoflakes, and 3-D nanocanyons with specific preferential orientations normal to the insulated SiO_2/Si substrates were newly fabricated. Most significantly, this is the first time that such many featured and well-aligned Bi_2Te_3 nanostructures have been fabricated and reproduced by a single deposition process. Moreover, this approach not only provides controllable microstructures but also overcomes many technological issues, such as the pollution of the residual templates or catalysts and the oxidation of the formed nanostructures. In order to obtain reliable thermoelectric related data and to evidence well-aligned nanostructures as an advanced strategy, the thermoelectric properties were confirmed with independent characterization equipment and methods. This paper is expected to provide a better comprehension of the relation between the in-plane thermoelectric properties and structural characteristics and to offer a promise for realizing high-ZT thermoelectric nanostructures.

Experimental

Nanostructure deposition

The Bi_2Te_3 powders were dry pressed into discs of 10 mm diameter and 2 mm thickness and were then annealed under hydrogen atmosphere at 20 Torr at 300 °C for 10 h. The X-ray diffraction (XRD) pattern of the sintered target confirmed the existence and the crystal structure of the single phase Bi_2Te_3 (see ESI, Fig. S1†). In order to prevent the substrate effect on the following thermoelectric measurement, a SiO_2 layer with a thickness of 500 nm was thermally grown on Si substrates. The crystal structure and composition of the prepared targets for PLD were confirmed as those of the starting powders. A Q-switched Nd:YAG pulsed laser (Litron, LPY 664) with a focused laser fluence of about 8.3 J cm^{-2} (355 nm wavelength, 10 ns pulse duration, 8 mm beam diameter and 5 Hz repetition rate) was kept for the deposition processes. The deposition chamber was evacuated to a base pressure of 5×10^{-6} Torr and 99.999% purity Ar was then introduced for the pressure control at various substrate temperatures from 250 to 550 °C.

Structure analysis

The morphology, size, and composition of the well-aligned 0-D to 3-D Bi_2Te_3 nanocrystals were examined by field emission scanning electron microscopy (FE-SEM, JEOL JSM-6500) with energy disperse spectroscopy (EDS, Oxford). The orientation and crystallinity of these four Bi_2Te_3 nanostructures were determined by XRD (Bruker AXS, D8 Discover) with CuKα radiation ($\lambda = 1.54$ Å) in θ–2θ configuration and transmission electron microscopy (TEM, JEOL JEM-2100 and JEM-3000F). The oxidation state of the Bi_2Te_3 nanostructures was characterized by X-ray photoelectron microscopy (XPS, Thermo VG 350).

Thermoelectric characterization

The current–voltage (I–V) curve and the electrical conductivity of the Bi_2Te_3 nanostructures were respectively measured from the two-probe (Keithley 2400) and four-probe methods (CMT SR2000N) with gold electrodes. The corresponding carrier concentration and mobility were examined with a Hall system (Accent HL5500). The cross-section SEM images provided the accurate thicknesses needed. The Keithley 2400 was utilized to provide thermal energy on one side of the specimen, and a maximum temperature gradient of 16 °C was then created between two electrodes with an interval of 1.0 cm. The Seebeck voltage and temperature difference were recorded *in situ* and plotted for obtaining the Seebeck coefficients. The contribution of the thermocouple wires (Cu leads) has been subtracted from the absolute Seebeck coefficients obtained.

Results and discussion

Fig. 1 shows the cross-section and top view SEM images of the nanoblock assembled Bi_2Te_3 films deposited at various substrate temperatures, revealing uniform featured nanocrystals which can be respectively identified as 0-D nanoparticles, 1-D nanorods, 2-D nanoflakes, and 3-D nanocanyons. The corresponding size distributions were statistically counted from the SEM images. The 0-D nanoparticles deposited at 300 °C were pretty dense with an average diameter of 19 nm (see Fig. 2(a)). The 1-D nanorods deposited at 250 °C were perpendicularly aligned to the substrates with a height of ~1400 nm and an average width of ~130 nm for the square-like cross-section as can be seen in Fig. 2 (b). Similarly, the 2-D nanoflakes formed at 500 °C were also aligned perpendicularly to the substrates (Fig. 1(c)). A special cross-link between these nanoflakes can be clearly observed in Fig. 1(g). The mean width, thickness and height were 690, 56, and 1740 nm, respectively, as shown in Fig. 2(c). The 3-D nanocanyons which consist of layered structures deposited at 550 °C

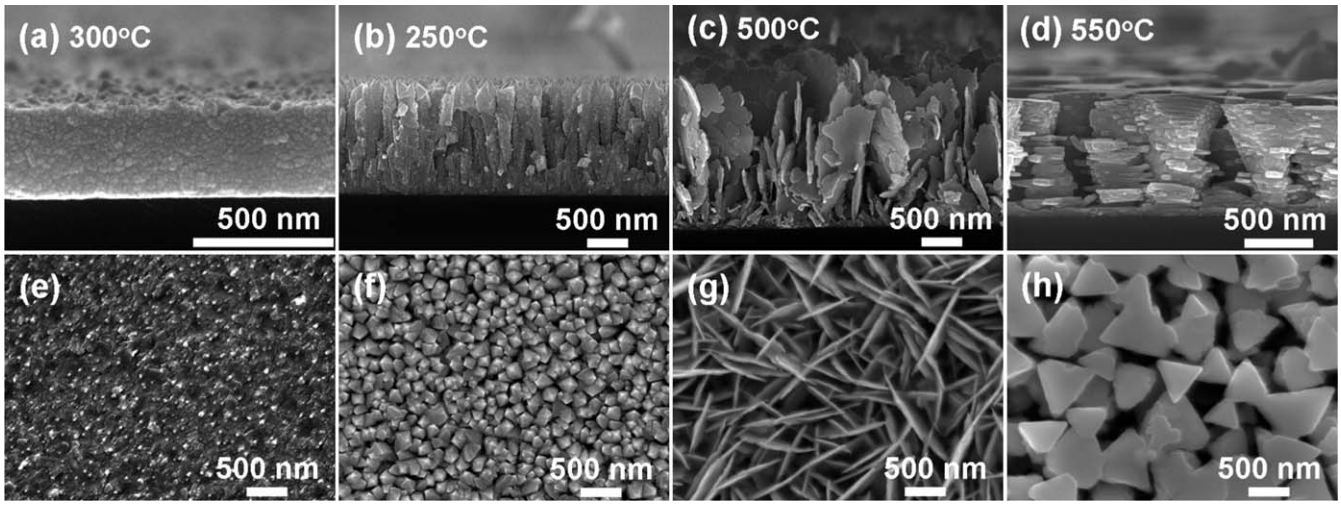

Fig. 1 The cross-section SEM images of the (a) 0-D nanoparticles, (b) 1-D nanorods, (c) 2-D nanoflakes, and (d) 3-D nanocanyons assembled Bi_2Te_3 nanostructures deposited at 300, 250, 500, and 550 °C for 3 h, respectively. The corresponding top view SEM images are shown in (e)–(h).

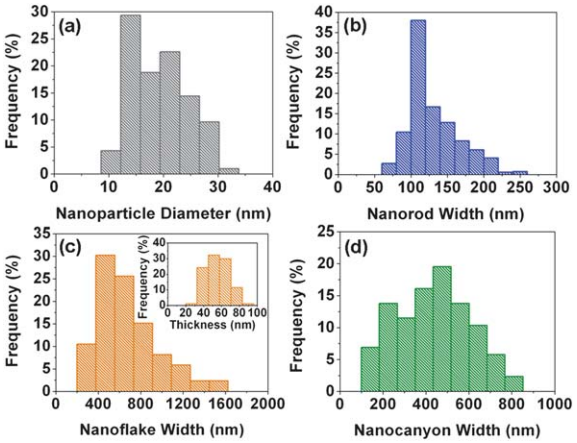

Fig. 2 The size distributions of (a) the diameter of the nanoparticles (cross-section SEM image), (b) the width of the square-like cross-section of the nanorods, (c) the width and thickness (inset) of the nanoflakes, and (d) the width of the nanocanyons. (b)–(d) were obtained from the top view SEM images.

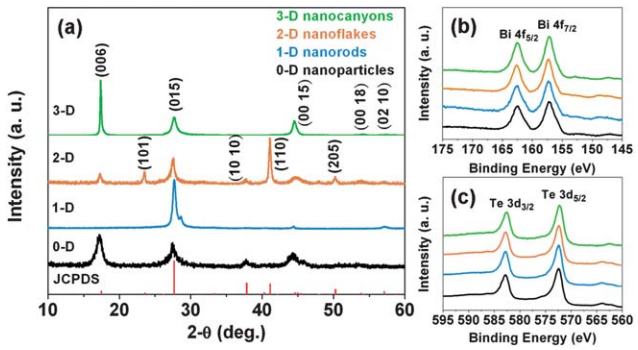

Fig. 3 (a) XRD patterns recorded for the well-aligned 0-D to 3-D Bi_2Te_3 nanostructures formed at various deposition temperatures. The indexed reflections correspond to the rhombohedral Bi_2Te_3 (JCPDS 89-4302). The corresponding XPS spectra of the (b) Bi 4f and (c) Te 3d state evidence the absence of oxidation states.

have a stacking height of ~880 nm (Fig. 1(d)). The triangle-like top view (Fig. 1(h)) has an average width of ~440 nm (Fig. 2(d)).

According to the XRD patterns as shown in Fig. 3(a), all these four nanostructures can be mainly identified as the Bi_2Te_3 rhombohedral phase (JCPDS 89-4302) with respective out-of-plane preferential orientations. It is surprising that the recorded peaks for 0-D nanoparticles seem perfectly random, however, the relatively high integrated intensity of the (006) peak indicates the occurrence of the anisotropic growth. For the well-aligned 1-D nanorods, the (015) direction clearly dominated the out-of-plane preferential growth. An impurity peak found neighbor to Bi_2Te_3(015) was identified as Te(101) (JCPDS 89-4899), which might originate from the more volatile behavior of the Te element in PLD.[19] For the 2-D nanoflakes, the (110) peak is determined as the preferential orientation by numerical analysis with other peaks. In contrast to the (015) and (110) preferential orientations for the nanorods and nanoflakes, respectively, the 3-D nanocanyons display a strong *c*-axis preferential orientation, *i.e.* (006). The chemical composition and binding energy of these four nanostructures were evaluated by EDS and XPS, respectively. Four elements, Bi, Te, Si and O can be clearly observed in the EDS spectra. The deviation of the Bi/Te composition (see Table 1) with the substrate temperatures is frequently observed in various deposition techniques. The binding energy of 157.2 eV and 162.5 eV shown in Fig. 3(b), and of 572.2 eV and 582.5 eV in Fig. 3(c) can be indexed as the $4f_{7/2}$ and $4f_{5/2}$ band for Bi^0, and $3d_{5/2}$ and $3d_{3/2}$ band for Te^0, respectively. The absence of the oxidation states for both Bi and Te is in agreement with the XRD observations and will be the merit for their electrical conductivity.

The cross-section TEM images of the well-aligned 0-D to 3-D nanostructures are shown in Fig. 4(a)–(d), and the square marks the region for the selected-area electron diffraction (SAED) as displayed in Fig. 4(e)–(h). The slightly diffused SAED spots indicate that each morphological unit of the Bi_2Te_3 nanostructures excluding 0-D is not a perfect single crystal but is an ordered assembly of nanocrystals with slight misorientations. According to the mean size (see Fig. 2(a)), the region selected for

Table 1 The EDS chemical composition of the well-aligned 0-D to 3-D Bi_2Te_3 nanostructures

Composition	0-D Nanoparticles	1-D Nanorods	2-D Nanoflakes	3-D Nanocanyons
Bi (at%)	40	38	43	45
Te (at%)	60	62	57	56

SAED may contain only few 0-D nanoparticles. Thus, a clear ring pattern cannot be observed even though the stacks of the 0-D nanoparticles are quite random as mentioned in Fig. 3(a). As can be seen in Fig. 4(b), the head of the 1-D nanorods is tetrahedral-like and the clear diffused (015) spots shown in Fig. 4(f) are in agreement with the out-of-plane orientation determined by XRD. From Fig. 4(c), the triangle-like shape of one piece of the free-standing 2-D nanoflakes can be clearly seen and the Moiré fringes marked by the dash circle prove the existence of the small angle grain boundaries within the nanoflakes. In addition, the pair of (110) diffraction spots and the relatively unobvious diffraction spots, (101), (015) and (205) appearing in Fig. 4(g) indicate the (110) out-of-plane preferential orientation. In the case of the 3-D nanocanyons, the Moiré fringes also can be observed in Fig. 4(d) and the corresponding slightly diffused SAED pattern (Fig. 4(h)) should originate from the minor stacking misorientations in both out-of-plane and in-plane directions.

Here we briefly summarize the structural investigations as plotted in Fig. 5 that the Bi_2Te_3 nanocrystals including 0-D nanoparticles, 1-D nanorods, 2-D nanoflakes, and 3-D nanocanyons were formed and well-aligned at 300, 250, 500, and 550 °C with an overall (006), (015), (110), and (006) preferential orientation, respectively. In the PLD process, the melting, vaporization, and ablation induced by the high-energy pulsed laser may occur simultaneously to form a plasma plume[20] on the surface of a rotating Bi_2Te_3 target. In this work, in order to keep the film composition, the operating ambient pressure was adjusted from $\sim 6.6 \times 10^{-3}$ Torr to ~ 1.3 Torr corresponding to various substrate temperatures. It has been experimentally evidenced that when the ambient pressure is around 1 Torr or higher, nanoparticles are condensed in the plasma plume before they reach the substrate.[21,22] Generally, the condensed particle size is very tiny, *e.g.* 2.4 nm Pt nanoparticles produced by PLD at

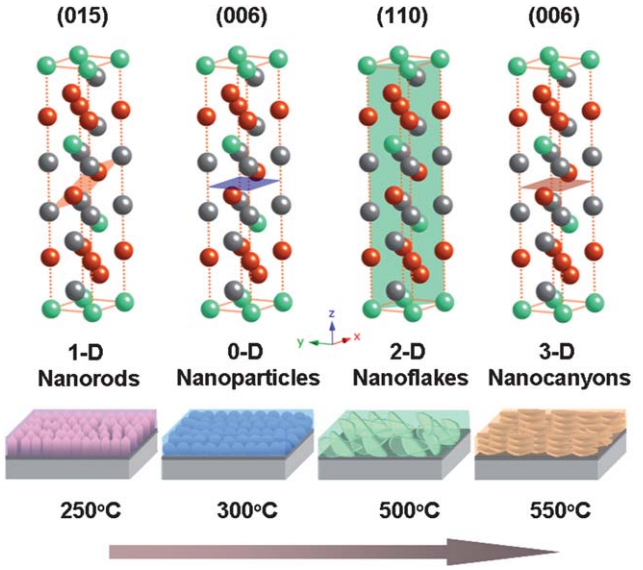

Fig. 5 Illustration of the preferential orientation, the dimension of the nanocrystals and the alignment with respect to the substrates under various deposition temperatures ranging from 250 to 550 °C. The gray, green, and red spheres represent the Bi, $Te^{(1)}$, and $Te^{(2)}$ atom positions, respectively.

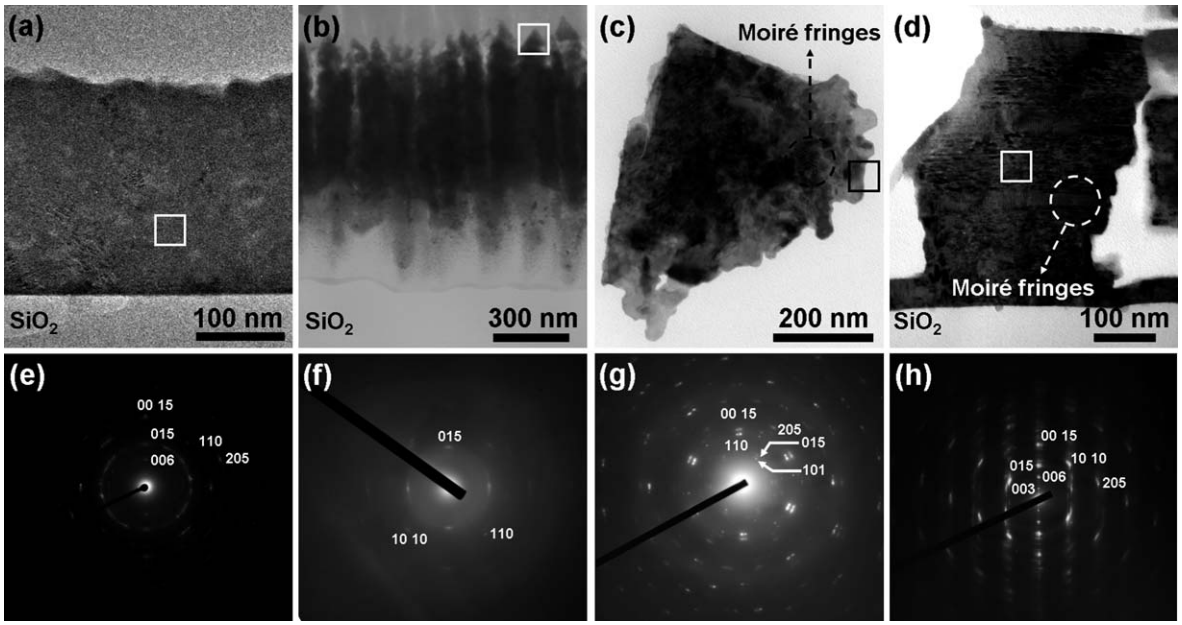

Fig. 4 The cross-section TEM images of the (a) 0-D nanoparticles, (b) 1-D nanorods, (c) 2-D nanoflakes, and (d) 3-D nanocanyons. The corresponding SAED patterns taken from the squared region are shown in (e)–(h).

an ambient pressure of 0.8 Torr, and depends on the sampling parameters.[21]

The granular structures of the 0-D nanoparticle film formed at a substrate temperature of 300 °C and an ambient pressure of $\sim 1.5 \times 10^{-1}$ Torr thus can be considered as the assembly of the gas-phase condensed Bi_2Te_3 nanoparticles. However, if the ambient pressure is the only structure-controlling factor, then the nanoparticle assemblies should be quite random instead of having preferential orientation as clearly observed in the XRD pattern (see Fig. 3(a)). Considering the substrate temperature (300 °C) which is about half of the melting temperature of Bi_2Te_3 bulk (T_m = 573 °C),[6] it is reasonable to believe that the kinetic energy of the deposited nanoparticle atoms, given by the substrate temperature governs the ability to overcome the diffusion barriers.[23] The diffusion processes between the condensed Bi_2Te_3 nanoparticles can thus actively occur and lead to the formation of larger dense and oriented nanoparticle aggregates. As a result, at a given temperature, these diffusion barriers should control the evolution of film morphology as well as the orientation during the growth. In the case of 1-D nanorods, since the ambient pressure was kept at $\sim 6.6 \times 10^{-3}$ Torr which is about two to three orders of magnitude lower than other cases, the Bi_2Te_3 plasma species should not be greatly condensed in the gas phase. The growth of the 1-D nanorod film might thus be mainly ruled by the interaction between the Bi_2Te_3 plasma species and the substrate surface. Under this frame, the 1-D column structure can be well predicted from the substrate temperature (250 °C = $\sim 0.4\ T_m$) by applying the structure zone models (SZM).[24]

Since the 2-D nanoflakes (500 °C) and the 3-D nanocanyons (550 °C) were grown respectively at ambient pressures of $\sim 7.0 \times 10^{-1}$ Torr and ~1.3 Torr, as discussed above, the gas-phase condensed Bi_2Te_3 nanoparticles should be the main material source for supplying the film growth. When the nanoparticles reached the high-temperature substrates (slight lower than T_m), atoms in the nanoparticles should get energy to exhibit a very high diffusion ability. In order to minimize the surface energy created by the landing nanoparticles, the atoms should spontaneously diffuse toward the prior formed crystals from their landing locations to give the growth of 2-D or 3-D nanoblocks.

Here we further propose another growth mechanism that might also occur under the present deposition condition. When the condensed nanoparticles land on the high-temperature substrates, if the landing nanoparticles are tiny enough, they might immediately melt due to the nanosize induced reduction of the melting point. The melted nanoparticles might diffuse their atoms to the prior formed crystals and solidify. At the same time, the melted nanoparticles might also act as the self-catalysts to assist the crystal growth by following the vapor–liquid–solid (VLS) growth mechanism[25,26] where the Bi_2T_3 plasma species could be the vapor source. Similar nanoparticle assisted crystal growth by PLD at a relatively high substrate temperature with self-catalysis has also been reported.[27]

Observing the morphology (see Fig. 1) as well as the crystalline orientation (see Fig. 4) of the 2-D and 3-D blocks, it is clear that the growth of both the featured crystal blocks was determined at the very initial deposition stage. In the present experiments, since all the substrates were placed at the same position, orientation effects due to the geometry of the vapor beam should not occur. From numerous experimental evidences, for instance, Bassi *et al.* have demonstrated a series of Bi_2Te_3 films prepared by PLD at an ambient pressure close to the present work and found that the (006) orientation tends to appear at higher deposition temperatures (>350 °C) otherwise (015) presents.[28] The studies on the sputtered Bi_2Te_3 films also present similar results that (006) is oriented above 400 °C whereas (015) dominates orientation below 250 °C.[29] Thus we believe that the (110) and (006) (the close packing plane) oriented growth should be also thermodynamically favored respectively at the substrate temperature of 500 °C and 550 °C. The film growth regarding the extremely high substrate temperatures for Bi_2Te_3 prepared by physical deposition techniques at relatively high ambient pressure is rather complex, which has been less reported and discussed.

In this work, all the thermoelectric properties were measured along the in-plane direction and shown in Table 2. The negative Hall coefficients confirm that electron-type carriers are dominant in all the prepared nanostructures. The carrier concentration of the 0-D nanoparticles ($\sim 9 \times 10^{19}$ cm^{-3}) is quite close to that of the 1-D nanorods and is higher than that of the 2-D nanoflakes and 3-D nanocanyons ($\sim 2 \times 10^{19}$ cm^{-3}) since Te is volatile at higher deposition temperatures[19] (see Table 1). The carrier mobility measured from the 0-D to 3-D Bi_2Te_3 nanostructures is 14.8, 2.0, 31.9, and 19.5 cm^2 V^{-1} s^{-1}, respectively. The *I–V* curve showed excellent linearity over the entire range of applied voltages and indicated that the contacts are ohmic (see Fig. 6(a)). The slope of the four Bi_2Te_3 nanostructures yielded the resistance of 590, 790, 230, and 124 Ω, respectively. We further determined the electrical conductivities from the four-probe method as 230, 29, 78, and 70 S cm^{-1}, which are close to the results of the Hall measurement. The Seebeck coefficient (see Fig. 6(b)) for the 0-D to 3-D Bi_2Te_3 nanostructures exhibits similar levels with that for intrinsic Bi_2Te_3 bulk, which also confirms their n-type semiconductor behavior. Higher deposition temperatures (2-D and 3-D) seem important for obtaining higher Seebeck coefficients where the averaged values are −91, −81, −132, and −143 μV K^{-1} for the 0-D to 3-D, respectively. However, the electrical conductivity would be generally sacrificed with the Seebeck coefficient increasing due to the opposite tendency for these two parameters. Moreover, it is worthy to mention that, increase of the 0-D nanoparticle film thickness from ~350 nm to ~1.1 μm

Table 2 Room-temperature thermoelectric properties of the well-aligned 0-D to 3-D Bi_2Te_3 nanostructures

Thermoelectric properties	0-D Nanoparticles	1-D Nanorods	2-D Nanoflakes	3-D Nanocanyons
Carrier concentration (10^{19} cm^{-3})	9.70	9.14	1.52	2.24
Carrier mobility/cm^2 V^{-1} s^{-1}	14.8	2.0	31.9	19.5
Electrical conductivity/S cm^{-1}	230	29	78	70
Seebeck coefficient/μV K^{-1}	−91	−81	−132	−143
Power factor/μW cm^{-1} K^{-2}	1.90	0.19	1.35	1.43

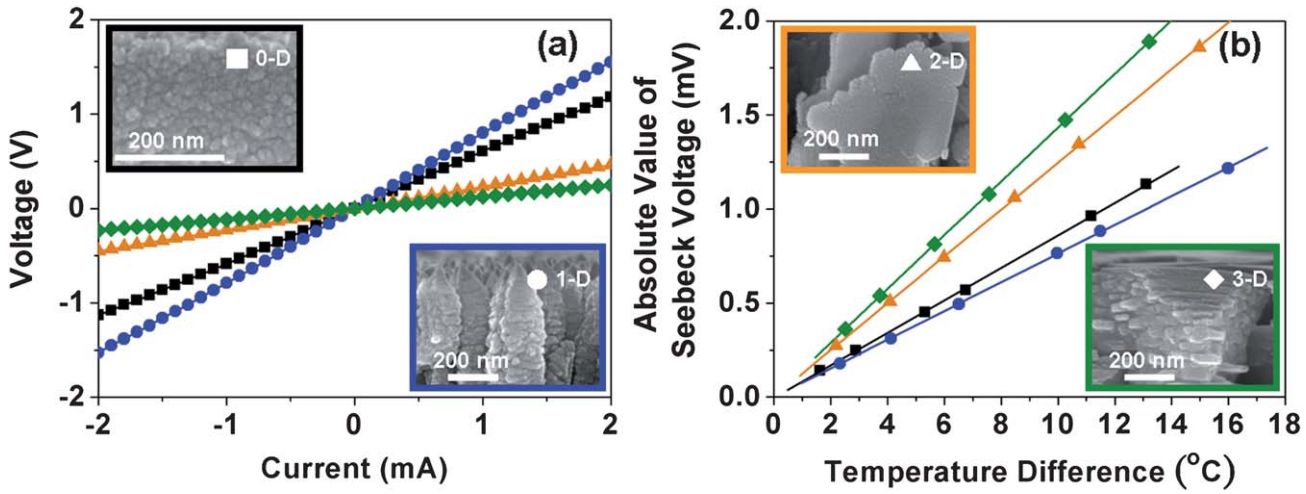

Fig. 6 (a) The *I–V* curve and (b) the Seebeck voltage plotted as a function of the temperature difference across the well-aligned 0-D to 3-D Bi_2Te_3 nanostructures. Insets are the corresponding cross-section SEM images.

seems to lead to only very slight changes of the electrical conductivity and Seebeck coefficient (see Fig. S2, S3, and Table S1†). Thus, according to these direct experimental evidences, we consider that for 0-D nanoparticle film, the thickness is not an effective factor for changing or modifying the thermoelectric properties.

The in-plane power factors are 1.90, 0.19, 1.35, and 1.43 μW cm^{-1} K^{-2} respectively for the 0-D to 3-D nanostructures as shown in Table 2. The present dry synthesis process is considered to provide clean and solid contacts between nanoparticles (see Fig. 3(b) and (c)). Thus the relatively high electrical conductivity and power factor can be obtained. For instance, the present dense 0-D nanoparticle (~19 nm diameter) films exhibit about eight times higher electrical conductivity but only ~40% lower Seebeck coefficient comparing with the sintered pellets completely consisted of nanoparticles (~39 nm diameter).[13] In addition to the grain conductance, of course the particle size would also be an important issue. When the nanoparticle size of the pellets decreases to sub-10 nm,[12] a further enhancement in ZT was experimentally found mainly due to the three times increase in the electrical conductivity but only ~11 μV K^{-1} decrease in magnitude in the Seebeck coefficient comparing with the present 0-D nanoparticle films. The decrease of the Seebeck coefficient with grain size has similar tendency as the theoretical prediction by Glatz and Beloborodov.[30] It is generally believed that the well alignment is of critical importance for 1-D nanostructures to present distinct properties. The power factor of the well-aligned 1-D nanorods is significantly enhanced in comparison with that of the randomly aligned quantum rods (~70 nm in diameter synthesized by chemical processes).[10] Greatly improved electrical conductivity of the well-aligned 1-D nanorods would be the point as discussed in the 0-D nanoparticles. Similarly, Deng and Xiang also showed competitive data measured from the Bi_2Te_3 quantum-wire arrays (prepared by vacuum deposition).[9] From the SEM images (Fig. 1), the well-aligned 2-D nanoflakes exhibit much more porous assemblies than the 0-D and 1-D nanostructures. It is thus not expected to have an excellent electrical conductivity which is considered as the most critical parameter for most assembled nanostructures. But the good alignment is still helpful for the contribution of the electrical conductivity, comparing with the randomly aligned nanoflakes[9] and the microspherical bouquet with 2-D nanoplates.[17] In contrast to the foregoing structures, the well-aligned 3-D nanocanyons have not been previously reported and showed an excellent power factor only inferior to 0-D nanoparticles. The relatively high electrical conductivity is still the main reason. We believe that air-filled interspaces may be an effective medium for resisting phonon transport and thus further improve the performance of thermoelectric thin films.

Conclusions

In summary, we have successfully demonstrated the systematic fabrication of physically self-assembled and well-aligned Bi_2Te_3 nanostructures on SiO_2/Si substrates without pre-built templates or catalysts by PLD at various substrate temperatures ranging from 250 to 550 °C. The building nanocrystals of the prepared Bi_2Te_3 nanostructures were clearly identified as the 0-D nanoparticles, 1-D nanorods, 2-D nanoflakes, and 3-D nanocanyons and were found to be well-aligned on SiO_2/Si substrates with overall (006), (015), (110), and (006) preferential orientations, respectively. The substrate temperature and ambient pressure may play the key roles to influence the growth mechanism and the corresponding orientation and morphologies. The well-aligned 0-D to 3-D Bi_2Te_3 nanostructures show excellent in-plane power factors of 1.90, 0.19, 1.35, and 1.43 μW cm^{-1} K^{-2}, respectively. It is worth to notice that most of the randomly aligned intrinsic Bi_2Te_3 nanostructured films generally present values smaller than 1 μW cm^{-1} K^{-2} at room temperature. The experimental evidence proved that the significant improvement in the power factor mainly originates from the reduction of the inter resistance.

Acknowledgements

Financial support from the National Science Council of the Republic of China under grant NSC-99-2221-E-009-041 is gratefully acknowledged.

Notes and references

1 M. S. Dresselhaus, G. Chen, M. Y. Tang, R. Yang, H. Lee, D. Wang, Z. Ren, J.-P. Fleurial and P. Gogna, *Adv. Mater.*, 2007, **19**, 1043.
2 B. Poudel, Q. Hao, Y. Ma, Y. C. Lan, A. Minnich, B. Yu, X. Yan, D. Z. Wang, A. Muto, D. Vashaee, X. Y. Chen, J. M. Liu, M. S. Dresselhaus, G. Chen and Z. F. Ren, *Science*, 2008, **320**, 634.
3 B. C. Sales, *Science*, 2002, **295**, 1248.
4 L. D. Hicks and M. S. Dresselhaus, *Phys. Rev. B: Condens. Matter Mater. Phys.*, 1993, **47**, 12727.
5 L. D. Hicks and M. S. Dresselhaus, *Phys. Rev. B: Condens. Matter Mater. Phys.*, 1993, **47**, 16631.
6 D. Teweldebrhan, V. Goyal and A. A. Balandin, *Nano Lett.*, 2010, **10**, 1209.
7 J. Ham, W. Shim, D. H. Kim, S. Lee, J. Roh, S. W. Sohn, K. W. Oh, P. W. Voorhees and W. Lee, *Nano Lett.*, 2009, **9**, 2867.
8 D. M. Rowe, *Thermoelectrics Handbook: Macro to Nano*, CRC, 2005, pp. 20.
9 Y. Deng, Y. Xiang and Y. Song, *Cryst. Growth Des.*, 2009, **9**, 3079.
10 A. Purkayastha, F. Lupo, S. Kim, T. Borca-Tasciuc and G. Ramanath, *Adv. Mater.*, 2006, **18**, 496.
11 R. Venkatasubramanian, E. Siivola, T. Colpitts and B. O'Quinn, *Nature*, 2001, **413**, 597.
12 M. Scheele, N. Oeschler, K. Meier, A. Kornowski, C. Klinke and H. Weller, *Adv. Funct. Mater.*, 2009, **19**, 3476.
13 M. R. Dirmyer, J. Martin, G. S. Nolas, A. Sen and J. V. Badding, *Small*, 2009, **5**, 933.
14 A. Purkayastha, S. Kim, D. D. Gandhi, P. G. Ganesan, T. Borca-Tasciuc and G. Ramanath, *Adv. Mater.*, 2006, **18**, 2958.
15 H. Yu, P. C. Gibbons and W. E. Buhro, *J. Mater. Chem.*, 2004, **14**, 595.
16 A. Purkayastha, Q. Yan, M. S. Raghuveer, D. D. Gandhi, H. Li, Z. W. Liu, R. V. Ramanujan, T. Borca-Tasciuc and G. Ramanath, *Adv. Mater.*, 2008, **20**, 2679.
17 T. Wang, R. Metha, C. Karthik, P. G. Ganesan, B. Singh, W. Jiang, N. Ravishankar, T. Borca-Tasciuc and G. Ramanath, *J. Phys. Chem. C*, 2010, **114**, 1796.
18 W. Lu, Y. Ding, Y. Chen, Z. L. Wang and J. Fang, *J. Am. Chem. Soc.*, 2005, **127**, 10112.
19 A. Bailini, F. Donati, M. Zamboni, V. Russo, M. Passoni, C. S. Casari, A. L. Bassi and C. E. Bottani, *Appl. Surf. Sci.*, 2007, **254**, 1249.
20 M. N. R. Ashfold, F. Claeyssens, G. M. Fuge and S. J. Henley, *Chem. Soc. Rev.*, 2004, **33**, 23.
21 D. Riabinina, E. Irissou, B. L. Drogoff, M. Chaker and D. Guay, *J. Appl. Phys.*, 2010, **108**, 034322.
22 A. B. Hartanto, X. Ning, Y. Nakata and T. Okada, *Appl. Phys. A: Mater. Sci. Process.*, 2004, **78**, 299.
23 C. R. Henry, *Surf. Sci. Rep.*, 1998, **31**, 231.
24 J. A. Thornton, *J. Vac. Sci. Technol. (N. Y., NY, U. S.)*, 1974, **11**, 666.
25 W. Shi, R. W. Hughes, S. J. Denholme and D. H. Gregory, *CrystEngComm*, 2010, **12**, 641.
26 C. Xu, D. Kim, J. Chun, K. Rho, B. Chon, S. Hong and T. Joo, *J. Phys. Chem. B*, 2006, **110**, 21741.
27 T. Okada and J. Suehiro, *Appl. Surf. Sci.*, 2007, **253**, 7840.
28 V. Russo, A. Bailini, M. Zamboni, M. Passoni, C. Conti, C. S. Casari, A. L. Bassi and C. E. Bottani, *J. Raman Spectrosc.*, 2008, **39**, 205.
29 M. H. Francombe, *Philos. Mag.*, 1964, **10**, 989.
30 A. Glatz and I. S. Beloborodov, *Phys. Rev. B: Condens. Matter Mater. Phys.*, 2009, **79**, 041404–041408 (R).

